Biosensors and Bioelectronics 142 (2019) 111485

Contents lists available at ScienceDirect

Biosensors and Bioelectronics

journal homepage: www.elsevier.com/locate/bios

# Integration of rolling circle amplification and optomagnetic detection on a polymer chip

Francesca Garbarino[a], Gabriel Antonio S. Minero[a], Giovanni Rizzi[a], Jeppe Fock[b], Mikkel Fougt Hansen[a,*]

[a] Department of Health Technology, Technical University of Denmark, DTU Health Tech, Building 345C, DK-2800, Kongens Lyngby, Denmark
[b] Blusense Diagnostics ApS, Fruebjergvej 3, DK-2100, Copenhagen, Denmark

ARTICLE INFO

*Keywords:*
Lab-on-a-chip
Nucleic acid analysis
Microfluidics
Magnetic nanoparticles
Magnetic microparticles

ABSTRACT

Rolling circle amplification (RCA) combined with padlock probe recognition of a DNA target is attractive for on-chip nucleic acid testing due to its high specificity and isothermal reaction conditions. However, the integration of RCA on an automated chip platform is challenging due to the different reagents needed for the reaction steps and the temperature sensitivity of the phi29 polymerase. Here, we describe the integration of an RCA assay on a single-use polymer chip platform where magnetic microbeads are used as solid support to transport the DNA target between three connected reaction chambers for (i) padlock probe annealing and ligation, (ii) RCA, and (iii) optomagnetic detection of RCA products. The three chambers were loaded with reagents by sequential filling combined with passive microfluidic structures. After loading, the on-chip assay steps were automated. For an assay in which all steps but the padlock probe annealing on the target were performed on-chip, we found a limit of detection (LOD) for a synthetic influenza target of 2 pM after 45 min of RCA, which is comparable to the corresponding laboratory assay. The entire assay, including padlock probe annealing, could be performed on-chip with an LOD of 20 pM after 45 min of RCA. This LOD can likely be reduced by further optimizing the microbead mixing. The results present important steps towards the integration and automation of RCA and potentially also other complex multi-step assays on a single-use polymer chip for molecular analysis.

## 1. Introduction

Microfluidic devices have the potential to miniaturize laboratory analyses and to drastically reduce sample and reagent volumes and thereby the cost of a biomolecular test (Giuffrida and Spoto, 2017). Moreover, new passive approaches to liquid handling have greatly reduced the complexity and increased the robustness of these devices. Among these are capillary-stop valves based on sudden channel expansions (Cho et al., 2007; Gottheil et al., 2014) and phaseguide structures used to control the liquid spreading in chambers to avoid trapping of air-bubbles (Vulto et al., 2011).

An important application for microfluidic devices is lab-on-a-chip detection of nucleic acid targets (Maffert et al., 2017). Polymerase chain reaction (PCR) has become an essential tool for *in vitro* amplification of nucleic acid sequences (Maffert et al., 2017; Ahrberg et al., 2016), but the fast and precise temperature cycling needed for the reaction is demanding in a low-cost lab-on-a-chip setting. Therefore, there has been significant interest in alternative isothermal molecular amplification strategies (Zhao et al., 2015; Duan et al., 2016; Deng and Gao, 2015). These methods include recombinase polymerase amplification (RPA) (Piepenburg et al., 2006), loop-mediated isothermal amplification (LAMP) (Tomita et al., 2008), and rolling circle amplification (RCA) (Ali et al., 2014).

High specificity and sensitivity are key requirements for DNA detection in molecular diagnostics. Exponential amplification techniques such as LAMP and RPA can detect few copies of DNA molecules, but they are also prone to false-positive results that can be particularly difficult to control in an out-of-lab setting (Minero et al., 2017). In contrast, linear amplification by RCA can amplify the DNA target sequence a thousand fold in 1 h, making it ideal for many applications that require reliable analysis at the expense of a higher limit of detection (LOD) (Ali et al., 2014). In RCA, a circular template is formed by annealing and ligation of a padlock probe (PLP) on the target (Nilsson et al., 2002). Subsequently, the 3′-end of the DNA target is continuously extended on the PLP by phi29 polymerase to create a long single-stranded DNA concatamer containing repeated copies of the sequence complementary to the PLP. The formation of the circular template is highly sensitive to sequence mismatches near the point where the PLP is

* Corresponding author.
*E-mail address:* mfha@dtu.dk (M.F. Hansen).

https://doi.org/10.1016/j.bios.2019.111485
Received 30 April 2019; Received in revised form 26 June 2019; Accepted 28 June 2019
Available online 03 July 2019
0956-5663/ 

joined and can be designed to have 100% specificity for point mutations (Nilsson et al., 2002; Pavankumar et al., 2016).

In the past decade, magnetic microbeads (MMBs) have been used in nucleic acid assays for purification, amplification and detection (Dahl et al., 2004; Berensmeier, 2006; Tamanaha et al., 2008; Gijs et al., 2010; Van Reenen et al., 2014). Magnetic separation of RCA products constitutes a key step in so-called circle-to-circle (C2CA) amplification in which one or several additional cycles of RCA are used to increase the sensitivity of RCA (Dahl et al., 2004; Göransson et al., 2012; Neumann et al., 2018). Hernández-Neuta et al. recently presented an on-chip RCA assay combining a fluidized bed of MMBs with detection on a polymer microarray with an LOD of 1 pM after 20 min of RCA followed by 60 min of C2CA (Hernández-Neuta et al., 2018).

We have previously achieved an LOD of 10 pM after 1 h of RCA using an optomagnetic (OM) readout method (Bejhed et al., 2015; Donolato et al., 2015). This method is attractive for use in disposable chips as it only requires a transparent sample container and can be made from comparatively low-cost components such as a data collection card, a light emitting diode and a small electromagnet. The OM method probes the second harmonic modulation of the intensity of light transmitted through a suspension of magnetic nanoparticles in response to a magnetic field of frequency $f$ applied along the light path (Fock et al., 2017a, 2018). The resulting spectra reflect the rotational diffusion properties of the particles, which are inversely related to their hydrodynamic size. When MNPs bind to the RCPs, their hydrodynamic size increases significantly and spectral features shift to lower frequencies (Donolato et al., 2015). Mezger et al. detected changes in the OM signal when two populations of functionalized MNPs were linked by single copies of the sequence complementary to the PLP (the RCP monomer) and found a monomer LOD of 30 pM (Mezger et al., 2015). Assuming a 1000-fold amplification during 1 h of RCA, this monomer LOD corresponds to a target LOD of 30 fM.

Herein, we present the integration and automation of a multi-step RCA assay on an all-polymer chip. This chip combines phaseguides and capillary stop valves to achieve controlled filling of liquids. The sample is handled on-chip using MMBs. The setup provides temperature control and automatic manipulation of the MMBs using external magnets. The on-chip operations comprise (1) PLP ligation, (2) RCA, and (3) optomagnetic detection. The results were found to be sensitive to the procedure for the annealing of the PLPs on the target. To study the potential for further improvement of the assay performance we therefore present and compare dose-response curves for two PLP annealing strategies where one is performed partly off-chip and the other is entirely performed on-chip.

## 2. Experimental section

### 2.1. Assay requirements

The PLP ligation, RCA and optomagnetic detection steps of the complete RCA assay carried out in this work required specific temperatures and buffers to work optimally. The optimal temperature for ligation is typically 5–10 °C below the melting points of the arms of the PLP-target hybrid where lower or higher temperatures result in unspecific PLP annealing or no PLP annealing, respectively, in both cases producing no template for RCA. In the present study, we used a ligation temperature of 58 °C (Minero et al., 2019). The RCA took place at 38.5 °C, but it was critical that the phi29 polymerase was not exposed to temperatures above room temperature prior to RCA as the free polymerase would otherwise be rapidly inactivated. In the present study, optomagnetic detection of the RCPs took place after RCA, where again a specific temperature and buffer were needed to produce optimum results.

To integrate and carry out the above assay on a chip, we therefore needed three separate chambers filled with different buffers and with different temperature requirements. As a key point, the chambers should be connected to enable transportation of the DNA target complex on MMBs between the chambers but with negligible liquid mixing between them. To fulfill these requirements, we developed the chip, setup and assay protocol described below. The filling sequence, setup and general experiment protocol are shown in the supporting information video.

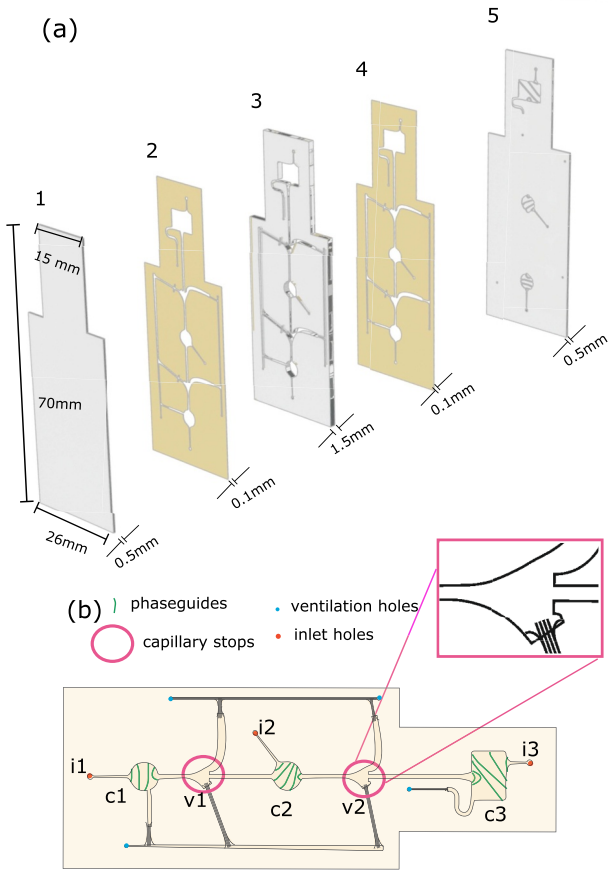


**Fig. 1.** (a) Bottom-to-top exploded view of the chip where parts 1 (bottom), 3 (middle), and 5 (top) are the **PMMA** layers of the chip and parts 2 and 4 are pressure sensitive adhesive foils mounted on the middle **PMMA** layer (part 3) during fabrication. (b) Schematic view of the chip design with labelled chambers (c1-c3), capillary valves (v1,v2), and inlets (i1-i3). The inset shows a zoom-in on the capillary valve.

### 2.2. Microfluidic chip

*Design.* The chip design (Fig. 1) was inspired by the multi-chamber chip with phaseguide and passive valve structures introduced by Gottheil et al. (2014). The chip was assembled from five layers (Fig. 1a) and contained three connected chambers (Fig. 1b). Two circular chambers (c1 and c2, ∅ 4.08 mm) and a rectangular chamber (c3, 5 × 7 $mm^2$) were connected by 0.6 mm wide channels with heart-shaped capillary stop valves (v1 and v2) with an abrupt expansion of the channel width (Fig. 1b, inset) (Cho et al., 2007). These were further connected to pressure ventilation and overflow channels placed near the chip sides. The chambers contained phaseguide structures (Vulto et al., 2011), ridges protruding from the top cavity of the chip (part 5 in Fig. 1a), to ensure controlled liquid filling without trapping of air bubbles.

*Fabrication.* Parts 1, 3 and 5 in PMMA defined the microfluidic structures and the lid of the chip in bottom-to-top order (Fig. 1a). Parts 2 and 4 were the 0.1 mm thick pressure sensitive adhesive (PSA) foils (ARcare 90106, Adhesive Research, Limerick, Ireland) placed on both

sides of part 3 prior to fabrication of the structures. All layers were structured by $CO_2$ laser ablation using vector cutting and engraving modes on an Epilog Mini 18 system. Part 5 was also processed in raster mode, using bi-directional engraving to remove material pixel by pixel to create a 40 $\mu$m deep cavity around phaseguide ridges (Garbarino et al., 2017) to enable controlled liquid filling in the chambers.

*Filling sequence.* The chip was loaded with the three different liquids in the three chambers by a c3-c2-c1 loading sequence (Fig. 1b and supplementary video). First, chamber c3 was loaded with liquid through inlet i3 using a pipette until the liquid reached valve v2. Excess liquid flowed into the overload channel just next to chamber c3. Then, inlet i3 was sealed using tape. Next, chamber c2 was loaded with liquid through inlet i2. Due to the design of the phaseguide structures, the liquid first filled the channel to valve v1 and then the channel connecting to valve v2. When it reached valve v2, the liquid continued to flow into the overflow channel (above v2 in Fig. 1b) and gas trapped in valve v2 could be released through a shallow pressure ventilation channel (below v2 in Fig. 1b). Then, inlet i2 was sealed using tape. Finally, chamber c1 was filled with liquid in the same manner and inlet i1 was sealed using tape.

Supplementary video related to this article can be found at https://doi.org/10.1016/j.bios.2019.111485

Fig. 2a shows the result of a loading sequence performed with dyed liquids. It is observed that the chambers are filled with the three different liquids with no mixing and that the regions where the liquids meet are separated from the chambers by at least 5 mm. This was sufficient to ensure that no mixing between the chambers took place during reactions due to diffusion. The heating of the different sections of the chip during the assay was found not to significantly shift any of the liquids.

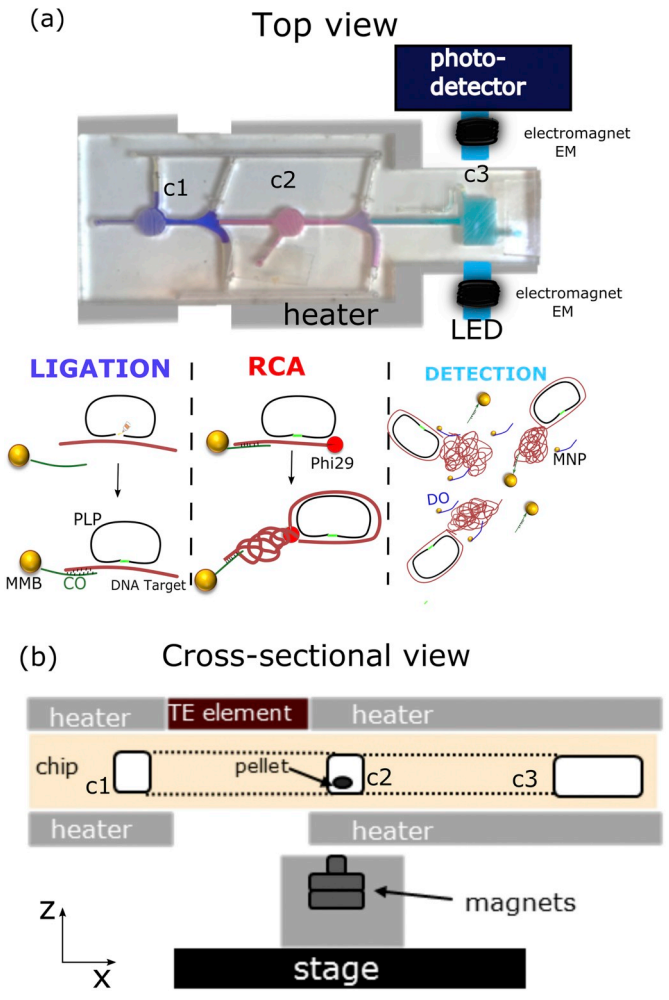


**Fig. 2.** (a) Top schematic view of the setup indicating the chambers and assay steps taking place in each chamber and a schematic of the optomagnetic setup. (b) Cross-sectional schematic view of setup indicating the positions of heaters, the three chambers and the external magnet.

### 2.3. Setup for integrated amplification and detection

Top and cross-sectional schematic views of the setup are given in Fig. 2. Pictures of the setup are given in Fig. S1.

*Magnetic manipulator.* The setup consisted of two motorized stages creating a two-axis ($xz$) stage with 50 mm horizontal travel (Thorlabs KBD101 driver and DDSM50/M linear stage) and 12 mm vertical travel (Thorlabs KDC101 driver and Z812B actuator mounted on an MPositioning T40Z-10A vertical stage). A custom milled aluminum magnet casing was placed on the top of the upper stage. The casing included a stack consisting of four axially aligned cylindrical magnets (top to bottom): two N48, NdFeB, ∅ 3 mm, 1 mm high magnets (S-03-01-N, Supermagnete, Gottmadingen, Germany) and two N45, NdFeB, ∅6 mm, 3 mm high magnets (S-06-03-N, Supermagnete, Gottmadingen, Germany) (Strohmeier et al., 2013). The magnets were used to manipulate the MMBs along the channel connecting the three chambers.

*Temperature control.* The stages were placed underneath two custom-built 2 mm thick resistive heaters where one set covered chamber c1 and the other covered chambers c2 and c3. Another identical set of heaters was placed on top to enable heating of the chip from both sides to ensure a faster and more precise temperature equilibration (Fig. 2b). The heaters were fabricated on aluminum printed circuit boards (PCBs) by defining the resistive heater wire as meandering circuits in the Cu layer. The temperature of each heater was monitored using Pt100 elements and controlled using a Stanford Research Systems PTC10 unit.

To avoid heating of chamber c2 with the temperature-sensitive phi29 polymerase above room temperature while heating chamber c1 during on-chip ligation, a 9 mm wide aluminum strip was placed between the two heaters on the top of the chip (Fig. 2b). The temperature of the aluminum strip was regulated and maintained at 25 °C using a thermoelectric (TE) element that was also controlled by the PTC10 unit. In subsequent assay steps, the temperature of this aluminum strip was set to the same temperature as the heater of chambers c2 and c3.

*OM detection setup.* The OM detection took place in chamber c3 (Fig. 2a and b). Light from a light emitting diode ($\lambda$ = 470 nm) was guided to the chip side and from the other side of the chip to a photodetector (Thorlabs PDA-36A-EC) using PMMA rods. Two electromagnetic coils placed symmetrically on either side of the detection chamber (c3) were used to produce a homogeneous oscillating magnetic field along the light path. The coils were driven by a custom-built voltage-to-current converter controlled by a data acquisition card (National Instruments, NI-6211) that also collected the signal from the photodetector.

### 2.4. Assay materials and protocol

*DNA sequences.* All DNA oligonucleotides were purchased from Integrated DNA Technologies, Belgium. Sequences are reported in the ESI†, Table S1. Experiments were carried out using a synthetic target DNA for type-B influenza virus (81 bases) (Neumann et al., 2018). The padlock probe (PLP, 90 bases, 5′-phosphate) was designed to match a specific sequence of the DNA target. A detection oligonucleotide (DO, 20 bases, 3′-biotin) was designed to be complementary to the RCPs and was attached to MNPs for OM detection. A capture oligonucleotide (CO, 15 bases of the recognition sequence, 3′-biotin) was attached to MMBs to enable capture and handling of the DNA target on the MMBs. The sequence was chosen to be outside the region targeted by the PLP. The length of the CO was adjusted so that the CO-target hybrid denatured in the detection buffer at temperatures above 54 °C, whereas the DO-RCP

hybrid was stable in the detection buffer up to 70 °C (Minero et al., 2019). This approach significantly increased the signal compared to a protocol where the RCPs were directly linked to the MMBs using a biotinylated DNA target (Fig. S2†) and was therefore used in the subsequent studies.

*Buffers and reagents.* Ampligase, BSA, dNTP mix and the 10× *Ligation buffer* (200 mM Tris-HCl (pH 8.3), 250 mM KCl, 100 mM MgCl2, 5 mM NAD, and 0.1% Triton X-100) were purchased from Nordic Biolabs. phi29 polymerase and 10× *RCA buffer* (330 mM Tris-acetate (pH 7.9), 100 mM Mg-acetate, 660 mM K-acetate, 1.0 % (v/v) Tween 20, 10 mM DTT) were purchased from Thermo Fischer. Additionally, we used the following buffers made from reagents from Sigma-Aldrich: *Binding buffer* (8 mM Tris-HCl (pH ≈ 8), 4 mM EDTA, 0.1 % Tween-20, and 0.8 M NaCl) and *Detection buffer* (20 mM Tris-HCL (pH≈ 8), 140 mM NaCl, 5 mM KCl, 50 mM EDTA, 0.1 % BSA, 0.01 % Tween20).

*Magnetic particles.* MyOne Streptavidin C1 magnetic microbeads (MMBs) from Thermo Fisher with a diameter of 1 $\mu$m were used for the capture and transportation of the DNA target complexes. Functionalization of the MMBs with CO probes was performed in a volume of 100 $\mu$L containing 12 $\mu$L MMB stock solution (10 mg mL$^{-1}$), 30 $\mu$L CO probes (1 $\mu$M) and 58 $\mu$L binding buffer. The suspension was end-over-end mixed for 30 min at room temperature. After 3 times washing and magnetic separation, the functionalized MMBs were re-suspended in a solution containing 80 $\mu$L MilliQ water, 10 $\mu$L ligation buffer (10×) and 10 $\mu$L BSA (2 mg mL$^{-1}$). MMB concentrations (in mg mL$^{-1}$) of 0.1, 0.2, and 0.3 were compared and the optimal value was found to be 0.2 (Section S3†).

The OM detection was carried out using multicore MNPs with a nominal diameter of 100 nm and a streptavidin surface (BNF-Starch streptavidin, prod. code 10-19-102, Micromod Partikeltechnologie GmbH, Germany). These MNPs have a remanent magnetic moment with a linked optical anisotropy (Fock et al., 2017a). A 50 $\mu$L volume of DO-probe functionalized MNPs was prepared by addition of 5 $\mu$L MNP stock solution (10 mg mL$^{-1}$) and 4 $\mu$L DO probes (1 $\mu$M) to 41 $\mu$L binding buffer. The suspension was placed in a tray for 30 min followed by 3 times magnetic separation and washing and finally resuspension in the detection buffer to a final MNP concentration of 0.05 mg mL$^{-1}$ used for OM detection.

*On-chip MMB handling.* During initial work, we found that the MMBs could interfere with the OM measurements on the MNPs in the detection chamber as MMBs in the light path produced a significant low-frequency signal with a tail that extended up to the frequency window used to quantify free MNPs (Fig. S4). It was therefore important to remove the MMBs from the light path. We found that the MMB pellet spread-out to a pancake-like shape when the magnet array was slowly moved away from the chip. The *z*-stage was introduced and was used in two positions, 'high' and 'low' corresponding to distances from the magnet top to the channel bottom of 3.5 and 15.5 mm, respectively. The 'high' position was used at all times, except when the magnets were to be moved away without dragging MMBs along. We found that lowering the magnet array to the 'low' position at 0.3 mm s$^{-1}$ resulted in a flat, spread out distribution of MMBs that no longer interfered with the OM measurements on the MNPs. The MMB spreading also had the positive effect that it was easier to release the RCPs bound to the MMBs. The MMBs were captured and manipulated on-chip using the motorized magnet assembly that could move the magnets along the fluid channel connecting the three chambers as well as in the vertical direction.

The *x*-stage was used to mix MMBs with the sample within a chamber and to transport MMBs between chambers. Mixing was performed by moving the stage back and forth between the edges of a chamber at alternating constant velocities ± 2 mm s$^{-1}$ (7 s in each direction) and served to increase the sample-MMB interaction and to minimize the risk of MMBs sticking to the bottom of the chamber. Mixing was performed during all incubation steps in the assay. Transportation was performed by moving the stage between chambers at 0.3 mm s$^{-1}$ with brief stops every 5 mm. This low velocity was chosen to ensure that all MMBs followed the moving magnet.

*Padlock probe annealing and ligation.* The PLP annealing and ligation consisted of (1) hybridization of the PLP to the target to form the padlock, and (2) enzymatic joining of PLPs on matching targets to form circles using ampligase. All target concentrations given below refer to the target concentration in the ligation mixture. The PLP was added in 3-fold excess to the target to minimize the number of unreacted probes (targets without circles). The PLPs were covalently joined in 1 × ligation buffer doped with BSA to 0.2 mg mL$^{-1}$ and Ampligase to 250 u mL$^{-1}$.

During the steps below, the heater of chambers c2 and c3 was off and the aluminum strip between c1 and c2 was kept at 25 °C to prevent heating of the temperature-sensitive phi29 polymerase above room temperature.

Two approaches for the PLP annealing with different level of on-chip integration were used and compared in the studies:

*'Off-chip PLP annealing':* The PLP was added to the target in the ligation buffer and placed in a thermoshaker without mixing at 55 °C for 20 min followed by cooling to 30 °C over 30 min. Ampligase and MMBs were added and the suspension was immediately loaded into chamber c1 on the chip. Under continuous MMB mixing, the temperature was kept at 58 °C for 20 min followed by cooling to 30 °C over 5 min to complete the ligation and target capture on the CO-functionalized MMBs.

*'On-chip PLP annealing':* Initial work revealed a reduced performance if the MMBs were present during the PLP annealing (Minero et al., 2018). Therefore, the MMBs were loaded in the RCA buffer and initially parked in chamber c2 and kept above the external magnet at the 'low' position. The PLP, target and ampligase were added to the ligation buffer and loaded in chamber c1 on the chip where the solution was incubated at 58 °C for 20 min. Then, the MMBs were transported to chamber c1 where they were kept under constant mixing at 58 °C for 2 min followed by cooling to 30 °C over 15 min to complete the ligation and target capture on the CO-functionalized MMBs.

*Rolling circle amplification.* The MMBs were transported from the ligation chamber (c1) to the RCA chamber (c2). Several concentrations of phi29 polymerase, dNTPs, BSA and RCA buffer were studied and optimized (Section S5†). As a result the RCA chamber was filled with 20 $\mu$L RCA buffer (10×), 20 $\mu$L BSA (2 mg mL$^{-1}$), 1.9 $\mu$L dNTPs (10 mM), 3 $\mu$L phi29 polymerase (10 u $\mu$L$^{-1}$), and 55.1 $\mu$L milliQ water. The RCA reaction took place at 38.5 °C for 45 min with continuous mixing of the MMBs. From each ligated PLP attached to an MMB, the RCA produced a single-stranded concatamer with nominally 750 copies of the sequence complementary to that of the PLP. The RCA product remained attached to the MMBs.

*Detection.* Upon completion of the RCA reaction, the temperature of chambers c2 and c3 was ramped towards the detection temperature of 56 °C. During the temperature ramping, the MMBs with attached RCPs were transported to the detection chamber (c3) containing the DO-functionalized MNPs in the detection buffer such that the MMBs entered the detection chamber (c3) when the heater temperature was about 50 °C. When the temperature stabilized at 56 °C, the *z*-stage was slowly lowered to the 'low' position at 0.3 mm s$^{-1}$. Then the *x*-stage was quickly moved to its home position furthest away from the detection chamber.

Subsequently, the second harmonic photodetector signal was measured as function of the frequency $f$ of the magnetic field $B(t) = B_0 \sin(2\pi ft)$ with $B_0$ = 1 mT. The sine and cosine components of the photodetector signal at $2f$, denoted $V_2'$ and $V_2''$, respectively, were found using a fast Fourier transformation algorithm. All measurements were normalized by the zero'th harmonic (average) photodetector signal $V_0$ to compensate for possible variations of the incoming light intensity. A single optomagnetic spectrum was obtained in 45 s by measuring the response at 41 logarithmically equidistant frequency points between 1 Hz and 2800 Hz (Fock et al., 2017a). The evolution of

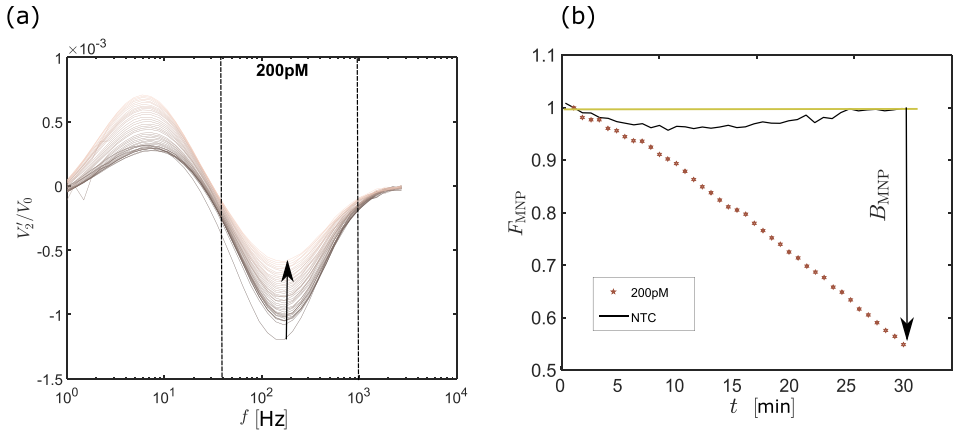


**Fig. 3.** (a) Time evolution of optomagnetic spectra measured during detection at 56 °C for $c$ = 200 pM in an experiment with off-chip PLP annealing. One spectrum was obtained every 45 s (increasing time indicated by arrow). The vertical dashed lines indicate the frequency range used to quantify the signal from free MNPs. (b) Relative change in signal from free MNPs, $F_{MNP}$ vs. detection time for the same sample and an NTC. The arrow indicates the fraction of bound MNPs, $B_{MNP}$, after 30 min of detection.

the spectra was studied over a detection period of 30 min corresponding to 40 measured spectra.

## 3. Results

### 3.1. Optomagnetic readout of integrated assay

Fig. 3a shows a series of OM spectra ($V_2'/V_0$ vs. $f$) obtained during detection after a complete experiment with off-chip PLP annealing for a target concentration of $c$ = 200 pM. The arrow indicates the time evolution of the spectra. The spectra show a negative peak centered at $f_{peak} \approx 150$ Hz and a positive peak at $f_{peak} \approx 5$ Hz. The OM method measures the ability of the MNPs to perform a small-angle rotation in response to the applied oscillating magnetic field, which is characterized by the Brownian relaxation frequency

$$f_B = \frac{k_B T}{\pi^2 \eta(T) D_h^3}. \quad (1)$$

Here, $k_B T$ is the thermal energy, $\eta(T)$ is the temperature-dependent viscosity of the liquid (=0.50 mPa s for water at 56°C), and $D_h$ is the apparent hydrodynamic MNP diameter. It has previously been established that the Brownian relaxation at low $B_0$-values gives rise to a peak in the $V_2'$-response at $f_{peak} = 1.21 f_B/\sqrt{3} \approx 0.70 f_B$ (Fock et al., 2018). Inserting the values of $f_{peak}$ found above, we estimate that the two peaks correspond to $D_h$-values of about 160 nm and 500 nm, respectively. The high-frequency peak observed between 50 Hz and 1 kHz in Fig. 3a (indicated by vertical lines) is attributed to free MNPs and the low-frequency peak is attributed to multiple MNPs attached to a single RCP. In the latter case, the peak has a positive sign due to optical interference phenomena appearing for clusters of MNPs (Fock et al., 2017b). As the detection time progressed in Fig. 3a, the peak from free MNPs decreased whereas that from bound MNPs increased as more and more MNPs attached to the released RCPs. Taking the first spectrum as representative for the initial suspension of MNPs, we define the relative signals $F_{MNP}$ and $B_{MNP}$ from free and bound MNPs, respectively, in spectrum number $n$ as

$$F_{MNP} = 1 - B_{MNP} = \frac{\sum_f V_2'(f, n)/V_0(f, n)}{\sum_f V_2'(f, 1)/V_0(f, 1)}. \quad (2)$$

where the sum is taken over frequencies $f$ between 50 Hz and 1 kHz.

Fig. 3b shows $F_{MNP}$ vs. time for the experimental data presented in Fig. 3a as well as for a no template control (NTC). The arrow indicates $B_{MNP}$ obtained after 30 min of detection that we will take as the binding signal in the following. For the shown 200 pM target concentration, we found $F_{MNP} \approx 0.55$, i.e., about 45% of the free MNPs were depleted from solution during the 30 min of detection.

In contrast, the NTC experiment in Fig. 3b had values of $F_{MNP}$, which deviated less than 3% from the nominal value of 1 during the detection and ended at a value after 30 min that was indistinguishable from 1, i.e., in this sample, virtually no free MNPs were depleted from solution during the 30 min detection.

### 3.2. Assay performance

Experiments were performed for DNA target concentrations of $c$ [pM] = 0, 1, 2, 4, 10, 20, 40, 100, 200, 400, 800 and 2000 for off-chip PLP ligation and $c$ [pM] = 0, 10, 20, 40, 100, 200, 400, 800, and 2000 for on-chip PLP ligation. Fig. 4 shows the fraction of bound MNPs after 30 min of detection, $B_{MNP}$, for the two experiment series (examples of $F_{MNP}$ signals vs. time are given in Fig. S6†). Error bars indicate the sample standard deviations (SD) obtained from three independent experiments. The horizontal signal cut-off lines indicate the NTC signal

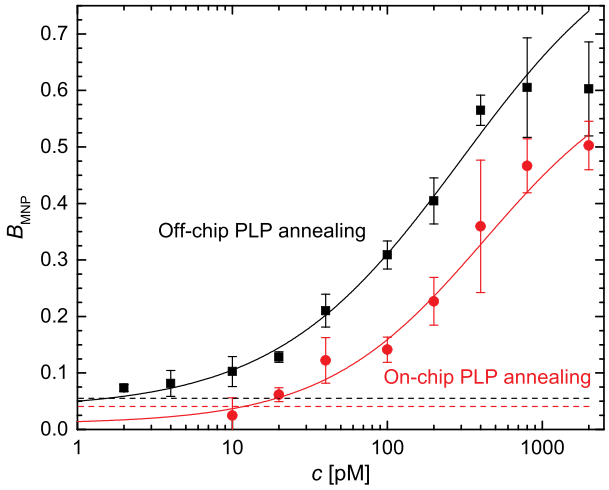


**Fig. 4.** Fraction of bound MNPs after OM detection for 30 min as function of DNA target concentration in experiments with off-chip PLP annealing (black squares) and on-chip PLP annealing (red circles). Error bars indicate the standard deviation based on three independent replicates ($n$ = 3). Horizontal lines indicate the signal cut-off taken as the NTC signal plus three SD. Solid lines are the fits to the Hill equation described in the text. (For interpretation of the references to colour in this figure legend, the reader is referred to the Web version of this article.)

plus three SD. The first target concentration for which the signal was higher than the cut-off line was taken as the limit of detection (LOD). The solid lines are fits to the Hill equation $B_{MNP}(c) = B_{MNP}(0) + [B_{MNP}(\infty) - B_{MNP}(0)]/[1 + (K_A/c)^{n_H}]$ with the association constant $K_A$ and Hill coefficient $n_H$.

For off-chip PLP annealing, we found an NTC signal of $B_{MNP}$= 0.007 ± 0.016, an LOD of 2 pM, $K_A$ = 146 pM and $n_H$ = 1.10. For on-chip PLP annealing, we found an NTC signal of $B_{MNP}$= 0.004 ± 0.012, an LOD of 20 pM, $K_A$ = 293 pM and $n_H$ = 1.28.

The two dose-response curves had similar cut-off values. The ten times higher LOD obtained for on-chip PLP annealing was therefore mainly due to the observation that the $B_{MNP}$-values for on-chip PLP annealing were generally about 0.1 lower than those obtained for off-chip PLP annealing. Thus, for off-chip PLP annealing more MNPs were bound to RCPs. For the investigated concentrations, both dose-response curves were observed to approach saturation with a slightly higher $B_{MNP}$-value of 0.6 for off-chip PLP annealing compared to that of 0.5 for on-chip PLP annealing.

## 4. Discussion

In the above results, off-chip PLP annealing produced significantly higher signals than on-chip PLP annealing. This indicated that fewer RCPs formed for on-chip PLP annealing, which could be due to a lower output of successful annealing and ligation or simply that fewer targets with ligated PLPs were captured on the MMBs. The PLP annealing and ligation were performed differently in the two strategies: either sequentially (off-chip annealing) or simultaneously (on-chip annealing). In standard RCA, however, these steps are usually performed simultaneously, so the fact that the steps were performed sequentially for the off-chip annealing should not affect the outcome. The reason is more likely to be found in the MMB handling. For off-chip annealing, the MMBs were mixed with the target-PLP complexes prior to on-chip capture and ligation. Therefore the MMBs had a higher chance of capturing the DNA targets compared to when the MMBs were only mixed with the DNA targets using the motion of the magnet.

These observations agree with the findings of Hernández-Neuta et al. (2018), who found that mixing using an actuated magnet was less efficient than their fluidized MMB bed. Moreover, for the on-chip annealing, the MMBs were parked (with the magnet under the second chamber at 'low' position) in the RCA buffer with the phi29 polymerase during the 20 min annealing at 58 °C. This procedure could result in some clustering of the MMBs, which would also make the subsequent capture of the target DNA less efficient.

In the dose-response analysis, results obtained for higher target concentrations tended to also have higher standard deviations. We believe that this is also due to limitations of the current MMB mixing protocol. During MMB mixing, the MMBs form a dense pellet at the bottom of the chip, which is moved back and forth using the external magnet resulting in a rolling motion of the MMBs. This inhomogeneous mixing gives rise to higher variability in the amount of DNA targets captured on the MMBs to be carried further to RCA and detection. Another source of variation between experiments is that occasionally a small amount of MMBs was left behind after MMB transportation between the chambers (Fig. S3b).

Hernández-Neuta et al. (2018) optimized the on-chip MMB mixing with the use of external pressure-driven liquid supplies. They were able to regulate the flow and liquid composition to achieve an LOD of the integrated system of 1 pM after two cycles of RCA. In contrast, we performed an initial loading of our chip with reagents and sample after which the assay ran automatically with no enrichment step or need for extra supply of liquids. For our approach with off-chip annealing, the LOD of 2 pM was comparable to that obtained by Hernández-Neuta et al. In the past, linear RCA assays or their readouts were adapted to, for example, discs (≈ 100 pM LOD for 90 min RCA) (Heo et al., 2016), bioactive paper strips (100 pM LOD for 60 min RCA) (Ali et al., 2009), and microarrays (480 fM for 4 h RCA) (Nallur et al., 2001). Considering the RCA times, the LODs obtained in the present work compare well with those reported for less integrated systems.

The presented system has the advantage that it does not rely on external pumps and valves and the disadvantage that it requires manual filling of reagents prior to initiation of an experiment and only runs a single-plex experiment. The developed microfluidic chips require no additional processing steps such as biomolecule spotting, sensor integration or functionalization and are suited for fabrication by a low-cost mass-production method such as injection moulding. The microfluidic chip and setup can be readily adapted to other RCA-assay targets, such as urinary tract infections (Mezger et al., 2015) and antibiotic resistance in tuberculosis (Engström et al., 2013). Moreover, its design and operation are flexible such that it can be adapted to other multi-step isothermal assays (Zhao et al., 2015).

## 5. Conclusion

We presented and demonstrated an automated on-chip RCA assay on a multi-chamber polymer chip with external chip temperature control and integrated capture, transportation and release of a DNA target complex by use of magnetic microbeads. The target was taken through ligation and rolling circle amplification to detection. The optomagnetic readout was based on measurements of the immobilization of functionalized magnetic nanoparticles on the rolling circle amplification products. Robust liquid handling was achieved using sequential filling of the three reaction chambers combined with capillary stops and phaseguide structures. Significant improvement in successful capture of target-ligated PLP complexes was found when targets were pre-annealed off-chip and were introduced on the chip after mixing with the MMBs. The dose-response curves were determined for assay protocols with off-chip or on-chip padlock probe annealing with limits of detection of 2 pM and 20 pM, respectively. These values obtained in a one-chip assay compare favorably to those obtained in similar but less integrated linear assays as well as MNP-based readout formats in previous studies.

Our future work aims to optimize the on-chip MMB mixing to improve the reproducibility of the assay results beyond the current proof of concept. The interaction between the MMBs and the sample can be enhanced using a cyclic magnetic field actuation sequence in which the MMBs are attracted to the top and bottom of the chamber, respectively. Such an approach has been demonstrated to be efficient in the literature (Bruls et al., 2009). In the present setup, we plan to realize this approach by adding an electromagnet on top of the top heater, which can be activated when the permanent magnet under the chip is in the 'low' position to create a force attracting the MMBs to the top of the chamber. Subsequently, the MMBs can be attracted to the chamber bottom by switching off the electromagnet and moving the permanent magnet under the chip to the 'high' position. Moreover, the sensitivity of the presented proof-of-concept can be further improved by implementing several cycles of RCA in a circle-to-circle amplification scheme. In this way, the sensitivity and risk of false positive results can be balanced to satisfy the need for a given application.

## Declaration of interests

The authors declare that they have no known competing financial interests or personal relationships that could have appeared to influence the work reported in this paper.

## CRediT authorship contribution statement

**Francesca Garbarino:** Data curation, Formal analysis, Investigation, Writing - original draft. **Gabriel Antonio S. Minero:** Conceptualization, Writing - review & editing, Methodology. **Giovanni Rizzi:** Conceptualization, Methodology. **Jeppe Fock:** Methodology,

Software, Writing - review & editing. **Mikkel Fougt Hansen:** Supervision, Conceptualization, Writing - review & editing, Methodology.

## Acknowledgement

We thank Mats Nilsson (SciLifeLab, Stockholm) for design of Influenza target and probes and Giada Violo (GV) for support on the chip fabrication. GV thanks Erasmus+ Program (Key action 1 A.Y. 2017-18) and Roberto Raiteri for sponsoring of the Erasmus program. We thank Bo Tian for a critical reading of the manuscript. The work was supported by DFF project (#4184-00121B) and MUDP (Grant No. MST-141-01415).

## Appendix A. Supplementary data

Supplementary data to this article can be found online at https://doi.org/10.1016/j.bios.2019.111485.

## References

Ahrberg, C.D., Manz, A., Chung, B.G., 2016. Lab Chip 16, 3866–3884. https://doi.org/10.1039/c6lc00984k.
Ali, M.M., Aguirre, S.D., Xu, Y., Filipe, C.D.M., Pelton, R., Li, Y., 2009. Chem. Comm. 43, 6640–6642. https://doi.org/10.1039/b911559e.
Ali, M.M., Li, F., Zhang, Z., Zhang, K., Kang, D.K., Ankrum, J.A., Le, X.C., Zhao, W., 2014. Chem. Soc. Rev. 43, 3324–3341. https://doi.org/10.1039/c3cs60439j.
Bejhed, R.S., Zardán Gómez De La Torre, T., Donolato, M., Hansen, M.F., Svedlindh, P., Strömberg, M., 2015. Biosens. Bioelectron. 66, 405–411. https://doi.org/10.1016/j.bios.2014.11.048.
Berensmeier, S., 2006. Appl. Microbiol. Biotechnol. 73, 495–504. https://doi.org/10.1007/s00253-006-0675-0.
Bruls, D.M., Evers, T.H., Kahlman, J.A., Van Lankvelt, P.J., Ovsyanko, M., Pelssers, E.G., Schleipen, J.J., De Theije, F.K., Verschuren, C.A., Van Der Wijk, T., Van Zon, J.B., Dittmer, W.U., Immink, A.H., Nieuwenhuis, J.H., Prins, M.W., 2009. Lab Chip 9, 3504–3510. https://doi.org/10.1039/b913960e.
Cho, H., Kim, H.Y., Kang, J.Y., Kim, T.S., 2007. J. Colloid Interface Sci. 306, 379–385. https://doi.org/10.1016/j.jcis.2006.10.077.
Dahl, F., Baner, J., Gullberg, M., Mendel-Hartvig, M., Landegren, U., Nilsson, M., 2004. Proc. Natl. Acad. Sci. U. S. A 101, 4548–4553. https://doi.org/10.1073/pnas.0400834101.
Deng, H., Gao, Z., 2015. Anal. Chim. Acta 283, 30–45. https://doi.org/10.1016/j.aca.2014.09.037.
Donolato, M., Antunes, P., de la Torre, T.Z.G., Hwu, E.T., Chen, C.H., Burger, R., Rizzi, G., Bosco, F.G., Strømme, M., Boisen, A., Hansen, M.F., 2015. Biosens. Bioelectron. 67, 649–655. https://doi.org/10.1016/j.bios.2014.09.097.
Duan, R., Lou, X., Xia, F., 2016. Chem. Soc. Rev. 45, 1738–1749. https://doi.org/10.1039/c5cs00819k.
Engström, A., Zardán Gómez de la Torre, T., Strømme, M., Nilsson, M., Herthnek, D., 2013. PLoS One 8, e62015. https://doi.org/10.1371/journal.pone.0062015.
Fock, J., Balceris, C., Costo, R., Zeng, L., Ludwig, F., Hansen, M.F., 2018. Nanoscale 10, 2052–2066. https://doi.org/10.1039/c7nr07602a.
Fock, J., Jonasson, C., Johansson, C., Hansen, M.F., 2017a. Phys. Chem. Chem. Phys. 19, 8802–8814. https://doi.org/10.1039/C6CP08749C.
Fock, J., Parmvi, M., Strömberg, M., Svedlindh, P., Donolato, M., Hansen, M.F., 2017b. Biosens. Bioelectron. 88, 94–100. https://doi.org/10.1016/j.bios.2016.07.088.
Garbarino, F., Kistrup, K., Rizzi, G., Hansen, M.F., 2017. J. Micromech. Microeng. 27, aa97b7. https://doi.org/10.1088/1361-6439/aa97b7.
Gijs, M.A., Lacharme, F., Lehmann, U., 2010. Chem. Rev. 110, 1518–1563. https://doi.org/10.1021/cr9001929.
Giuffrida, M.C., Spoto, G., 2017. Biosens. Bioelectron. 90, 174–186. https://doi.org/10.1016/j.bios.2016.11.045.
Göransson, J., Ke, R., Nong, R.Y., Howell, W.M., Karman, A., Grawé, J., Stenberg, J., Granberg, M., Elgh, M., Herthnek, D., Wikström, P., Jarvius, J., Nilsson, M., 2012. PLoS One 7, 1–9. https://doi.org/10.1371/journal.pone.0031068.
Gottheil, R., Baur, N., Becker, H., Link, G., Maier, D., Schneiderhan-Marra, N., Stelzle, M., 2014. Biomed. Microdevices 16, 163–172. https://doi.org/10.1007/s10544-013-9816-2.
Heo, H.Y., Chung, S., Kim, Y.T., Kim, D.H., Seo, T.S., 2016. Biosens. Bioelectron. 78, 140–146. https://doi.org/10.1016/j.bios.2015.11.039.
Hernández-Neuta, I., Pereiro, I., Ahlford, A., Ferraro, D., Zhang, Q., Viovy, J.L., Descroix, S., Nilsson, M., 2018. Biosens. Bioelectron. 102, 531–539. https://doi.org/10.1016/j.bios.2017.11.064.
Maffert, P., Reverchon, S., Nasser, W., Rozand, C., Abaibou, H., 2017. Eur. J. Clin. Microbiol. Infect. Dis. 36, 1717–1731. https://doi.org/10.1007/s10096-017-3013-9.
Mezger, A., Fock, J., Antunes, P., Østerberg, F.W., Boisen, A., Nilsson, M., Hansen, M.F., Ahlford, A., Donolato, M., 2015. ACS Nano 9, 7374–7382. https://doi.org/10.1021/acsnano.5b02379.
Minero, G.A.S., Cangiano, V., Garbarino, F., Fock, J., Hansen, M.F., 2019. Integration of microbead DNA handling with optomagneticdetection in rolling circle amplification assays. Microchim. Acta. https://doi.org/10.1007/s00604-19-3636-x.
Minero, G.A.S., Garbarino, F., Fock, J., Nilsson, M., Hansen, M.F., 2018. In: 12th International Conference on the Scientific and Clinical Applications of Magnetic Carriers, Poster 251.
Minero, G.A.S., Nogueira, C., Rizzi, G., Tian, B., Fock, J., Donolato, M., Strömberg, M., Hansen, M.F., 2017. Analyst 142, 3441–3450. https://doi.org/10.1039/c7an01023k.
Nallur, G., Luo, C., Fang, L., Cooley, S., Dave, V., Lambert, J., Kukanskis, K., Kingsmore, S., Lasken, R., Schweitzer, B., 2001. Nucleic Acids Res. 29, e118. https://doi.org/10.1093/nar/29.23.e118.
Neumann, F., Hernández-Neuta, I., Grabbe, M., Madaboosi, N., Albert, J., Nilsson, M., 2018. Clin. Chem. 64, 1–9. https://doi.org/10.1373/clinchem.2018.292979.
Nilsson, M., Gullberg, M., Dahl, F., Szuhai, K., Raap, A.K., 2002. Nucleic Acids Res. 30, e66. https://doi.org/10.1093/nar/gnf065.
Pavankumar, A.R., Engström, A., Liu, J., Herthnek, D., Nilsson, M., 2016. Anal. Chem. 88, 4277–4284. https://doi.org/10.1021/acs.analchem.5b04312.
Piepenburg, O., Williams, C.H., Stemple, D.L., Armes, N.A., 2006. PLoS Biol. 4, 1115–1121. https://doi.org/10.1371/journal.pbio.0040204.
Strohmeier, O., Emperle, A., Roth, G., Mark, D., Zengerle, R., Von Stetten, F., 2013. Lab Chip 13, 146–155. https://doi.org/10.1039/c2lc40866j.
Tamanaha, C.R., Mulvaney, S.P., Rife, J.C., Whitman, L.J., 2008. Biosens. Bioelectron. 24, 1–13. https://doi.org/10.1016/j.bios.2008.02.009.
Tomita, N., Mori, Y., Kanda, H., Notomi, T., 2008. Nat. Protoc. 3, 877–882. https://doi.org/10.1038/nprot.2008.57.
Van Reenen, A., De Jong, A.M., Den Toonder, J.M., Prins, M.W., 2014. Lab Chip 14, 1966–1986. https://doi.org/10.1039/c3lc51454d.
Vulto, P., Podszun, S., Meyer, P., Hermann, C., Manz, A., Urban, G.a., 2011. Lab Chip 11, 1596–1602. https://doi.org/10.1039/c0lc00643b.
Zhao, Y., Chen, F., Li, Q., Wang, L., Fan, C., 2015. Chem. Rev. 115, 12491–12545. https://doi.org/10.1021/acs.chemrev.5b00428.